PHYSICS OF FLUIDS **26**, 036602 (2014)

Radial intrusions from turbulent plumes in uniform stratification

Tamar S. Richards,[1] Quentin Aubourg,[2] and Bruce R. Sutherland[1,3,a)]
[1]*Department of Earth and Atmospheric Sciences, University of Alberta, Edmonton, Alberta T6G 2E3, Canada*
[2]*LEGI, Universite Joseph Fourier de Grenoble, Grenoble, France*
[3]*Department of Physics, University of Alberta, Edmonton, Alberta T6G 2E1, Canada*

(Received 26 September 2013; accepted 6 March 2014; published online 27 March 2014)

Laboratory experiments investigate the radial spread of an intrusion created by a turbulent forced plume in uniformly stratified ambient fluid. The flow evolution is determined as it depends upon the ambient buoyancy frequency, N, and the source momentum and buoyancy fluxes, M_0 and F_0, respectively. The plume reaches its maximum vertical extent, Z_m, collapses back upon itself as a fountain and then spreads radially outwards at its neutral buoyancy depth, Z_s, where the intrusion has the same density as the ambient. Through theory and experiments we determine that $Z_s = f(\sigma)H_p$, in which $H_p = M_0^{3/4}F_0^{-1/2}$, $\sigma = (M_0N/F_0)^2$, and $f(\sigma) \propto \sigma^{-3/8}$ for $\sigma \lesssim 50$ and $f(\sigma) \propto \sigma^{-1/4}$ for $\sigma \gtrsim 50$. In the inertia-buoyancy regime the intrusion front advances in time approximately as $R_f \propto t^{3/4}$, consistent with models assuming a constant buoyancy flux into the intrusion. Where the intrusion first forms, at radius R_1, its thickness h_1 is approximately constant in time. The thickness of the intrusion as a whole, $h(r, t)$, adopts a self-similar shape of the form $h/h_1 \simeq [(R_f - r)/(R_f - R_1)]^p$, with $p \simeq 0.55 \pm 0.03$. The comparison of these results to large volcanic plumes penetrating into and spreading in the stratosphere is discussed. © *2014 AIP Publishing LLC*. [http://dx.doi.org/10.1063/1.4869119]

I. INTRODUCTION

Volcanic eruptions cause the discharge of hot volcanic gases and particles that can penetrate vertically into the atmosphere up to tens of kilometers. Such eruptions have a convective column of three distinct regimes:[1] a gas thrust or jet region, an intermediate convective region, and an upper umbrella region. In the jet region, the effluent from the volcano rises primarily due to momentum. This region occurs over a small fraction of the total eruption column height. In the ensuing intermediate convective region, as the flow entrains ambient moisture and air it becomes controlled primarily by buoyancy forces. In the stratified atmosphere, the momentum and buoyancy fluxes decrease until the plume becomes negatively buoyant and ultimately reaches a maximum height where the momentum flux becomes zero. The plume then collapses upon itself as a fountain falling downward about the central rising plume until it reaches its neutral buoyancy level where the fluid originating from the plume has the same density as the surrounding ambient. From there it spreads radially outwards as an intrusive gravity current forming an umbrella region. For large volcanic eruptions, the influence of ambient winds can be ignored during the development of these three regimes as the umbrella region occurs in the stratosphere.[2]

Volcanic particles vary by several orders of magnitude, ranging from very fine submicron ash to particles larger than 1 m in diameter.[3] Larger particles leave the eruption column at lower levels,

a)Email: bruce.sutherland@ualberta.ca; URL: www.ualberta.ca/~bsuther.

while finer ash particles in the umbrella region can remain in the stratosphere for several days while spreading over the entire atmosphere. The spread of these particles can damage airplane engines[4] and can cause short-term cooling effects on climate.[5] Although simulations model the passive advection of particles by the synoptic scale winds, less well understood are the dynamics of the eruption column and the intrusion that emanates horizontally in its vicinity. Poorly constrained source conditions, the entrainment of moist air and the release of heat internally by particles within the eruption column are additional sources that provide buoyancy in the plume rise and spread.[6–8] Turbulence, high temperatures, and particles make it difficult to collect *in situ* data within the rising plume and its radial spreading region.[9] Likewise, the dynamics are too complex to be captured by direct numerical simulations. Nonetheless, insights have been gained through approximate theories guided by the results of laboratory experiments.[10]

The understanding of statistically steady turbulent forced plumes in uniform and stratified environments begins with the work of Morton *et al.*,[11] who derived equations for the evolution of volume, momentum, and buoyancy fluxes in a plume assuming that the lateral entrainment of the ambient into the plume at a particular height was proportional to the vertical speed of the plume at that height. Although highly successful in predicting the evolution of forced plumes in a uniform ambient, the predictions failed to predict the full evolution of a negatively buoyant plume because the entrainment assumption inaccurately captured the dynamics at the fountain top and consequent lateral entrainment of the descending fluid surrounding the plume core.[12,13] Nonetheless, a scaling analysis reveals how the height of a fountain depends upon the momentum and buoyancy fluxes at the source.[14–16]

Through theory and experiments of fountains in uniform stratification, Bloomfield and Kerr[13,17] examined the maximum and steady state rise height as well as the height at which the intrusion spreads. The theory, which assumed that momentum dominated over negative buoyancy at the plume source, provided good semi-empirical predictions of the spread height in this regime.

Even a buoyant plume eventually becomes negatively buoyant as inertia drives it past its neutral buoyancy level.[18] Then, like the starting-fountain study of Bloomfield and Kerr,[17] the resulting fountain eventually reaches a maximum height and falls back upon itself ultimately spreading radially as an intrusion.

Most theoretical and experimental studies of the radial spread of an intrusion in stratified fluid neglect the dynamics of the plume and collapsing fountain. Instead they assume a constant horizontal flux of volume, momentum, and buoyancy from a localized source.[19–23] Assuming that the volume flux and current height are constant and that the evolution is self-similar, the radius of the intrusion front is predicted[20] to increase in time as $R_f \propto t^{2/3}$. Taking into account the ambient stratification, Kotsovinos[23] instead predicted $R_f \propto t^{3/4}$.

There are relatively few studies examining the radial advance of an intrusion resulting from the collapse of a plume in uniformly stratified fluid. In an experimental study that focused upon internal wave generation by plumes in stratified fluid,[18] the intrusion front was found to advance radially as $R \propto R_f \propto t^{3/4}$ at early times. However, the analysis was limited to short times after the intrusion formed and detailed analyses of the intrusion structure and evolution were not performed.

This research revisits the problem of plume rise in stratified fluid but focuses upon the advance and structure of the intrusion as it propagates at its neutral buoyancy level. Unlike the experiments of Bloomfield and Kerr,[13,17] the buoyancy and momentum fluxes at the source have the same sign allowing us to examine intrusions emanating from buoyancy-dominated as well as momentum-dominated source conditions.

The theory for the rise and spread of a turbulent plume in a stratified ambient fluid are reviewed in Sec. II. The prediction for the spread height of Bloomfield and Kerr[17] is extended to include the influence of forced plumes dominated by buoyancy instead of momentum as they are influenced by the ambient stratification. The experimental setup and analysis are described in Sec. III. Section IV presents the quantitative results describing the radial advance and structure of the intrusions. In Sec. V, the results are summarized and compared to observations of large volcanic plumes penetrating into and spreading within the stratosphere.

II. THEORY

Although the motivation for this work is the examination of volcanic plume rise and spread in the stratosphere, it is convenient in laboratory experiments to examine a dense descending plume in uniformly stratified fluids. In the Boussinesq approximation, this circumstance is equivalent to a rising plume of less dense fluid. In reality, the density of the eruption column near the source can be vastly different than the ambient and the column itself propagates over more than one density scale height (about 8 km) as it passes into the stratosphere. Thus, the non-Boussinesq effects would play an important role in determining the plume rise.[10,24] However, our focus here is upon the transition of the plume into a collapsing fountain and the consequent radial spreading intrusion. These dynamics occur over a relatively small vertical distance within the stratosphere,[2,8] so that the Boussinesq approximation is reasonably applied. For simplicity in this study, we do not include the effect of particles within the plume, focusing instead upon the influence of buoyancy and inertia of the fluid associated with the plume and radial intrusion created.

The theory presented here is for a turbulent forced plume that initially moves downward in a uniformly stratified fluid, and consistent with our experimental setup as illustrated schematically in Figure 1. Fluid of density, ρ_0, greater than the surrounding ambient density ($\rho_0 > \rho_{00}$), is injected downward with volume flow rate, Q_0, from a source of radius, b_0. This falls to a maximum depth, Z_m, then rises as a fountain and finally spreads radially outwards at its neutral buoyancy level given by Z_s. The radius of the incident plume at Z_s is denoted by R_0. The radius at which the intrusion is first observed to propagate radially in the inertia-buoyancy regime is denoted by R_1. The radius of the intrusion front, which increases in time, is denoted by $R_f(t)$. Beyond a radius, R_v, the advance of the intrusion is dominantly influenced by a balance of viscosity and inertia.

The characteristics of a turbulent forced plume from an effectively point source are determined by the source momentum and buoyancy fluxes given, respectively, by[15]

$$M_0 = \pi b_0^2 w_0^2 \tag{1}$$

and

$$F_0 = \pi b_0^2 w_0 g_0' = Q_0 g_0'. \tag{2}$$

Here w_0 is the mean vertical velocity at the source,

$$w_0 = \frac{Q_0}{\pi {b_0}^2}, \tag{3}$$

and ${g_0}'$ is the reduced gravity at the source:

$${g_0}' = g\,\frac{\rho_0 - \rho_{00}}{\rho_{00}}, \tag{4}$$

in which g is gravity and ρ_{00} is the density of the ambient fluid at the nozzle depth. The definitions of w_0 and ${g_0}'$ are such that F_0 is positive, consistent with the understanding that buoyancy initially acts in the same direction at which the fluid is injected.

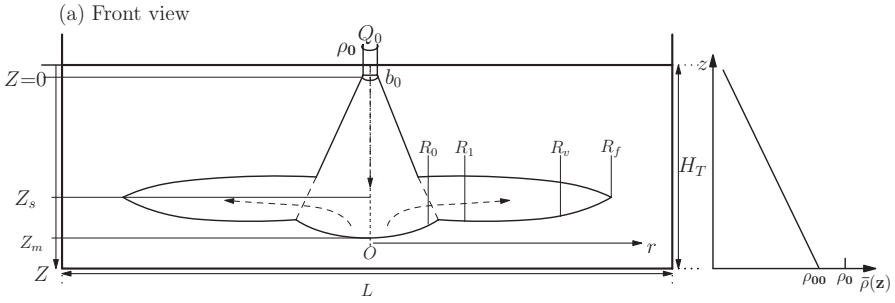

FIG. 1. Side view of a dense plume falling and spreading in a uniformly stratified environment.

From M_0 and F_0, dimensional arguments reveal the natural length scale of the system,[15]

$$H_p = M_0^{3/4} |F_0|^{-1/2}. \tag{5}$$

This is a measure of the vertical distance over which buoyancy overcomes the inertia associated with the flow at the source. In a uniform-density ambient if F_0 and M_0 have the same sign, H_p is the "jet length," determining the transition from jet-like to plume-like behaviour in a forced plume. If F_0 and M_0 have opposite sign, H_p is a measure of the rise height of a "forced fountain."[15,25]

In a uniformly stratified fluid, a forced plume eventually transforms into a fountain where it overshoots its level of neutral buoyancy. The maximum rise height and the consequent height of radial spreading depends not only upon H_p, but also upon the stratification expressed through the buoyancy frequency, N. In salt-stratified fluid N is given by

$$N = \sqrt{-\frac{g}{\rho_{00}} \frac{d\bar{\rho}}{dz}}, \tag{6}$$

in which $\bar{\rho}(z)$ is the background density, which decreases linearly with height, z, in a uniformly stratified Boussinesq fluid.

The relative influence of stratification is expressed through the nondimensional parameter, σ, defined by[13,17,26]

$$\sigma \equiv \frac{{M_0}^2 N^2}{{F_0}^2}. \tag{7}$$

The square root of σ is a measure of the time-scale for plume rise to H_p relative to the buoyancy period. If σ is large, the flow from the source remains jet-like as it is driven by momentum when stratification becomes important. But if σ is small, the flow is plume-like and driven by buoyancy when stratification becomes important.

Experiments of fountains in uniform-density and uniformly stratified fluids show that they first reach a maximum height before falling back toward the source. Thereafter the fountain top fluctuates about a steady state height, Z_m, moderately smaller than the initial maximum height.[15,17,18]

The spreading height, Z_s, of the radial intrusion is expected to scale with Z_m. In their experiments of negatively buoyant fluid injected upwards into uniformly stratified fluid, Bloomfield and Kerr[17] found $Z_s/Z_m \sim 0.51$. Here we examine how this relationship varies if the buoyancy flux of the source, with the same sign as the momentum flux, is non-negligible.

Just as Z_m should depend upon M_0, F_0, and N (or, equivalently, H_p and σ), so should the spread height, Z_s, of the radial intrusion. Both Z_m and Z_s can be estimated through numerical integration of the equations for a turbulent forced plume with constant entrainment proportional to the vertical speed at the plume center.[16,18,27] Here we consider the asymptotic limits of buoyancy-dominated and momentum-dominated sources. Following Bloomfield and Kerr,[17] we write the formula for the spread height as

$$Z_s = f(\sigma) H_p, \tag{8}$$

for some function, $f(\sigma)$. If $\sigma \ll 1$, stratification acts upon a buoyancy-driven flow and Z_s should be independent of M_0. Combining (5) and (7) so as to eliminate M_0 on the right-hand side of (8) gives the scaling relationship $f(\sigma) \propto \sigma^{-3/8}$. If $\sigma \gg 1$, stratification acts upon a momentum-driven flow and we instead eliminate F_0 on the right-hand side of (8) to get the scaling relationship $f(\sigma) \propto \sigma^{-1/4}$.

The second of these limits was derived by Bloomfield and Kerr,[17] who explicitly found through laboratory experiments that $f(\sigma) = 1.53\,(\pm\,0.10)\,\sigma^{-1/4}$, for $\sigma \gtrsim 100$. Their experiments of a fountain source (for which the source momentum and buoyancy fluxes were opposite signed) were not designed to explore the case of small σ. However, our study of a forced-plume source is designed to access both the small and large σ limits.

These limits have been explored previously[26] in experiments separately examining jet-like sources[28,29] and plume-like sources.[11] In particular, Caulfield and Woods[30] predicted for forced, pure or distributed plumes that the maximum rise height should scale as $Z_m \propto {F_0}^{1/4} N^{-3/4}$ $(= \sigma^{-3/8} H_p)$ if the flow rises well above the jet length ($\sigma \ll 1$). These studies focused upon the maximum rise height,

Z_m, not the spread height, Z_s. By determining the relationship between Z_m and Z_s for experiments with wide ranging σ, we are able to draw a connection between that body of work and our study of intrusions.

As well as determining the spread height, we wish to determine the structure and evolution of the radially spreading intrusion. Most studies of radially spreading intrusions ignore the dynamics of the plume and assume a source of uniform density fluid already at its neutral buoyancy level. This fluid emanates from a radius R_1, which is moderately larger than the radius, R_0, of the central plume at that height.

A straightforward application of self-similarity theory takes a box-model approach.[20] The speed, u_f, of the intrusion front with constant height, h_f, in uniformly stratified fluid is given by

$$u_f = \mathrm{Fr}\, N h_f, \tag{9}$$

in which the Froude number, Fr, is assumed to be constant. Shallow water theory and lock-release experiments of intrusions in uniformly stratified fluid predict[31–33] that $\mathrm{Fr} \simeq 1/4$. In its application to the intrusion spreading from the large volcanic eruption of Mount Pinatubo,[34] Fr was observed to be approximately 0.3.

To close the problem, we can make one of two assumptions about the source conditions at R_1. In one approach, we assume no entrainment into the intrusion so that the volume of the intrusion increases in time as

$$Q_i = 2\pi(R_f - R_1)h_f u_f \tag{10}$$

in which Q_i ($\simeq 2\pi R_1 h_1 u_1$) is the volume flux of the source emanating from a radius, R_1 with speed u_1 and thickness, h_1. Using this in (9) to eliminate h_f, the resulting equation for the advance of the intrusion front becomes[16,35,36]

$$\frac{dR_f}{dt} = u_f = \left(\frac{\mathrm{Fr}\, N Q_i}{2\pi}\right)^{1/2} (R_f - R_1)^{-1/2}.$$

Solving with the assumption that the front first forms at time, t_1 gives

$$R_{fQ} - R_1 \simeq \left(\frac{3}{2}\right)^{2/3} \left(\frac{\mathrm{Fr}}{2\pi}\frac{Q_i}{N}\right)^{1/3} [N(t - t_1)]^{2/3}. \tag{11}$$

This expression can be written in terms of the buoyancy flux, F_i, at R_1 through the relation

$$F_i \equiv Q_i g_i' \sim Q_i N^2 h_1, \tag{12}$$

in which h_1 is the depth of the intrusion at the source. In the box model $h_1 = h_f$, the depth of the intrusion over its length. Hence (11) becomes

$$R_{fQ} \simeq \left(\frac{3}{2}\right)^{2/3} \left(\frac{\mathrm{Fr}}{2\pi\, h_1}\frac{F_i}{N^3}\right)^{1/3} [N(t - t_1)]^{2/3}. \tag{13}$$

Substituting (11) back into (10) gives the intrusion height, which for $t \gg t_1$ and $R_f \gg R_1$ satisfies

$$h_{fQ} \propto t^{-1/3} \propto {R_f}^{-1/2}. \tag{14}$$

In a separate approach,[37] we suppose a constant buoyancy flux, F_i, from the source. We do not need to neglect the effects of entrainment in this case. While fluid entrained into the current head decreases its relative buoyancy, the head height also increases. Assuming the density of the entrained ambient fluid is approximately constant, the two effects conspire to maintain a constant buoyancy flux, if not volume flux. Using (10) and (12), the buoyancy flux at the source is

$$F_i \sim 2\pi N^2 (R_f - R_1){h_f}^2 u_f. \tag{15}$$

As above, we use this expression to eliminate h_f in (9) to get

$$\frac{dR_\mathrm{f}}{dt} = \left(\frac{\mathrm{Fr}^2\, F_i}{2\pi}\right)^{1/3} (R_\mathrm{f} - R_1)^{-1/3}.$$

From this it follows that

$$R_{\mathrm{f}F} - R_1 \simeq \left(\frac{4}{3}\right)^{3/4} \left(\frac{\mathrm{Fr}^2}{2\pi}\,\frac{F_i}{N^3}\right)^{1/4} [N(t - t_1)]^{3/4}. \tag{16}$$

This power law dependence, in the limit $t \gg t_1$, was also found[21,23] by assuming constant volume flux and balancing inertia and buoyancy forces written in terms of g', not N.

From (16) and assuming $t \gg t_1$ and $R_\mathrm{f} \gg R_1$, it follows that the intrusion height changes with time and front-radius as

$$h_{f\,F} \propto t^{-1/4} \propto R_\mathrm{f}^{-1/3}. \tag{17}$$

In both (14) and (17), the intrusion height (constant along its length) decreases in time. However, one does not expect the intrusion height at its source to be influenced by its downstream evolution. Assuming the source conditions are fixed and height, h_1, to be constant at R_1, we consider how the shape of the intrusion head influences the volume and buoyancy fluxes.

We suppose the depth, $h(r, t)$, of the intrusion along its radius adopts a self-similar shape of the form

$$h = h_1 \left(\frac{R_f - r}{R_f - R_1}\right)^{P_h}, \tag{18}$$

in which $R_\mathrm{f} = R_\mathrm{f}(t)$ and P_h is some constant exponent. The volume of the intrusion is

$$V = 2\pi \int_{R_1}^{R_\mathrm{f}} h\, r\, dr = \frac{2\pi h_1}{(P_h + 1)(P_h + 2)} \left[(R_\mathrm{f} - R_1)^2 + (R_\mathrm{f} - R_1)R_1(P_h + 2)\right]. \tag{19}$$

The buoyancy associated with the intrusion is

$$B = 2\pi N^2 \int_{R_1}^{R_\mathrm{f}} h^2\, r\, dr = \frac{\pi {h_1}^2 N^2}{(P_h + 1)(2P_h + 1)} \left[(R_\mathrm{f} - R_1)^2 + (R_\mathrm{f} - R_1)R_1(2P_h + 2)\right]. \tag{20}$$

The formulae predict that the volume and buoyancy increase as $R_\mathrm{f} - R_1$ increases in time. If the volume or buoyancy flux at R_1 is constant, then one expects

$$R_\mathrm{f} - R_1 \propto \begin{cases} t - t_1 & t \gtrsim t_1 \\ t^{1/2} & t \gg t_1 \end{cases}, \tag{21}$$

independent of the value of P_h. The transition from early to late occurs when the front is situated at $R_{\mathrm{f}c} \simeq R_1(3 + CP_h)$, with $C = 1$ assuming volume is conserved and $C = 2$, assuming buoyancy is conserved.

As well as testing whether the head structure indeed adopts a self-similar structure according to (18), the different predictions, (13), (16), and (21), for front position as a function of time are examined below.

III. SETUP, ANALYSIS METHODS, AND QUALITATIVE RESULTS

Laboratory experiments were conducted to gain insights into the spreading of an intrusion resulting from an axisymmetric buoyant plume collapsing to Z_s at its neutral buoyancy level in a stratified ambient. Experiments were conducted in one of two acrylic tanks: a cubical tank measuring 39.5 cm on each side and a wider tank measuring 120 cm long × 120 cm wide × 29.5 cm high. In both cases, the plume was injected downward into the centre of the tank, and the ambient stratification and source flow rate were established to ensure the plume did not impact the bottom of the tank before rising to its maximum height, then falling back to Z_s and intrudes radially outward.

A uniformly stratified ambient fluid was created using the double bucket technique.[38] The total ambient depth was $H_T \sim 30$ cm and 20 cm in the cubical and wide tanks, respectively.

The density profile of the ambient fluid created in the tank was recorded by taking samples at 5 cm intervals and measuring the densities with an Anton Paar DMA 4500 Densitometer. In some experiments, a vertically traversing conductivity probe (Precision Measurement Engineering MSCTI) was also used to measure the density profile of the ambient and the density profile across the spreading intrusion at a fixed position, $r > R_0$. The measured background density at corresponding heights confirmed a linear density profile for all experiments. The buoyancy frequency, N, produced a constant stratification ranging from 0.7 s^{-1} to 1.5 s^{-1} in different experiments.

The density of the plume at the source was established through the addition of salt to 3 l of water in a reservoir. In most experiments, the reservoir fluid was then dyed with red or blue food coloring then uniformly mixed. The resulting density of the source fluid, ρ_0, ranged from 1 g/cm^3 to 1.15 g/cm^3, as measured by the Densitometer. The fluid was injected downward into the tank through one of two nozzles with the opening 0.5 cm below the surface of the fluid. The small nozzle, of radius, $b_0 = 0.1$ cm, was fitted with a 0.05 cm mesh attached horizontally across the opening. The larger nozzle, of radius, $b_0 = 0.28$ cm, was fitted with six cross-wires spanning its opening. The mesh and cross-wires ensured that the flow leaving the nozzle was turbulent. Faster flow rates were achieved with the larger nozzle as the smaller nozzle only produced $Q_0 \lesssim 6$ cm^3/s.

Most experiments injected fluid from the reservoir through a centrifugal salt-water pump (HYDOR 200) with unimpeded flow rate, $Q = 328$ cm^3/s. The actual flow rate through the nozzle was controlled by adjustment of a clamp. The flow rate was measured by a flow meter (Muis Controls Ltd., P24/1-044-40C), and the desired flow rate through the nozzle was controlled by adjustment of the flow meter within the first 10 s of an experiment. In our experiments, the flow rate, Q_0, through the nozzle opening ranged from 3 cm^3/s to 12 cm^3/s.

Beside and behind the tank fluorescent light sources were positioned to illuminate the tank interior. White plastic sheets were placed on the outer walls of the tank to diffuse the incoming fluorescent light. A side view of the flow evolution was recorded by a digital video camera (Panasonic HDC HS250) that was positioned approximately 3 m from the front wall of the tank with the lens approximately at the vertical level of the intrusion. A still digital camera also recorded snapshots of the flow seen through the top of the tank, as shown in Fig. 2(d).

Each experiment lasted between 80 s and 290 s. At the end of each experiment, a square grid was positioned horizontally and vertically inside the tank so that the camera could record length scales for subsequent digital processing.

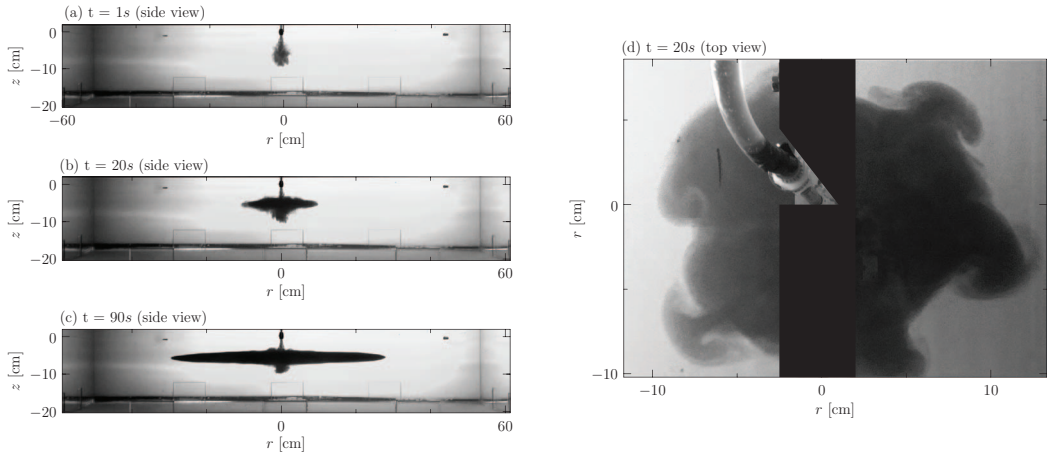

FIG. 2. Snapshots of an experiment performed in the wide tank with $N = 1.40$ s^{-1}, $\rho_0 = 1.020$ g/cm^3, $Q_0 = 7.4$ cm^3/s, and $b_0 = 0.28$ cm showing side views at times (a) $t = 1$ s, (b) $t = 20$ s, and (c) $t = 90$ s. (d) Top view of the experiment at $t \simeq 60$ s. (Multimedia view) [URL: http://dx.doi.org/10.1063/1.4869119.1].

Figure 2 shows snapshots taken at different times and perspectives of a typical experiment. As the plume initially moved downward away from the source, it expanded due to turbulent entrainment along the interface between the plume and ambient (Fig. 2(a)). As it moved further away, it became negatively buoyant, reached a maximum depth and collapsed back upon itself. This collapsing fluid reached its neutral buoyancy level (found at Z_s where the buoyancy flux vanishes) and then began to spread radially outwards (Fig. 2(b)). The front of the radially spreading intrusion advanced in time over the duration of the experiment (Fig. 2(c)). A top view of this experiment (Fig. 2(d)) showed that the spreading was not axisymmetric: azimuthal instabilities developed around the intrusion front. Such lobate structures were also observed to develop in the umbrella cloud emanating from the June 15, 1991, Mount Pinatubo eruption.[34] The analysis of these instabilities lies beyond the scope of this research. However, we found that analysis of the intrusions on either side of the central plume as recorded by the side-view camera was sufficient to characterize the mean speed and shape of the intrusion.

From snapshots taken at times after the intrusion were fully-developed (Fig. 2(c)), we measured the intrusion depth, $Z_s = 5.0\ (\pm\ 0.2)$ cm, and maximum plume depth, $Z_m = 9.0\ (\pm\ 0.1)$ cm. Assuming a linear spread with height of the forced plume near the source with spreading rate[39] 0.23, the virtual origin is situated $z_v \simeq 1$ cm above the nozzle opening. Thus, we define the distance from the virtual origin to the intrusion and maximum plume depth to be $Z_{sv} = 6.0$ cm and $Z_{mv} = 10.0$ cm, respectively.

To measure the formation and radial spread of the intrusion over time, we constructed horizontal time series taken at the spreading depth, Z_s, as shown in Figure 3. At early times shortly after the forced plume first passed the level Z_s, we identified the central plume radius, R_0. In this experiment, $R_0 = 1.0\ (\pm\ 0.3)$ cm.

At later times, the effects of azimuthal instabilities along the intrusion front (e.g., see Fig. 2(d)) were evident in the horizontal time series as thin regions of lower intensity light. These intensity variations and the difference between left- and right-propagating fronts were used to estimate the error of the front position, $R_f(t)$.

To aid in the determination of $R_f(t)$, the intensity contrast between the intrusion and ambient was enhanced. Using the image analysis software Matlab, an averaging filter was used to enhance the intensity contrast across the intrusion front measured in radial time series. Contours were then matched to the front position and the result smoothed. The co-ordinates of the resulting curve were extracted to form $R_f(t)$. The result is shown in Figure 4(a). This shows the intrusion front advanced radially outward though at a slower speed at later times ($t > 15$ s).

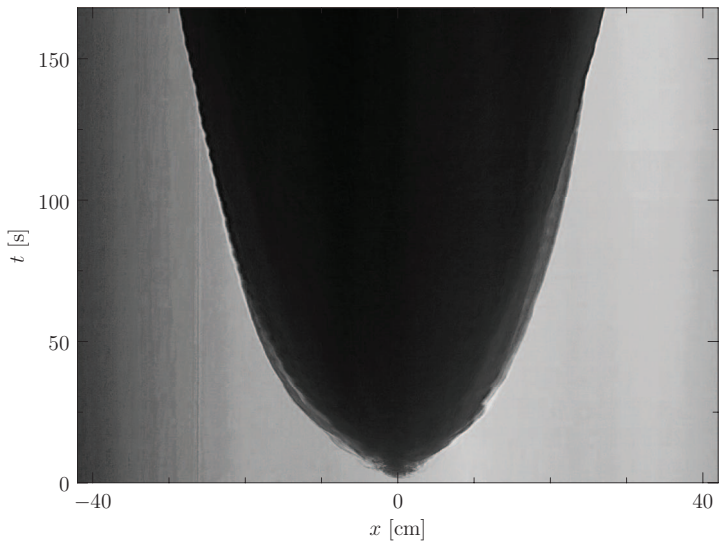

FIG. 3. Horizontal time series constructed from the experiment shown in Figure 2 with the time evolution being examined along a horizontal slice taken at the spreading level of the intrusion, $z = Z_s = 5$ cm.

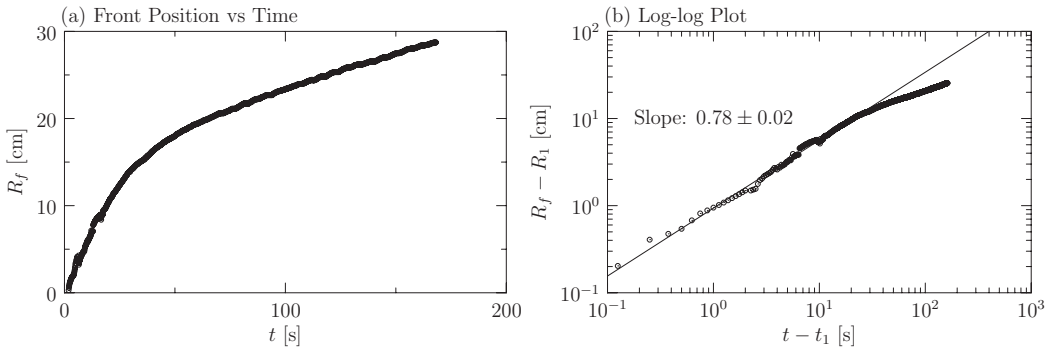

FIG. 4. From the horizontal time series shown in Fig. 3, plots of (a) the radial distance, R_f, of the intrusion front from the plume centerline as a function of time, t, with $t = 0$ corresponding to the start of the experiment. (b) The corresponding log-log plot of the radial distance of the intrusion front from its starting radius, R_1, as a function of the time, $t - t_1$, after the intrusion first develops in the inertia-buoyancy regime. The best-fit line to the data up to 10 s is shown in (b) with the value and error in its slope given at the upper left in (b).

The advance of the front exhibited two distinct regimes of behaviour as evident through the log-log plot shown in Figure 4(b). Here R_1 and t_1 are the radius and corresponding time, respectively, when the intrusion front first began to spread radially outward in the inertia-buoyancy regime. To determine R_1, we assumed that $\Delta R_f \equiv R_f - R_1$ versus $\Delta t \equiv t - t_1$ should follow a power law relationship for $R_f \gtrsim R_1$. Thus, we constructed a sequence of $\log(R_f - R')$ versus $\log(t - t')$ plots, in which R' ranged from R_0 to $5R_0$ and t' was defined implicitly by $R' = R_f(t')$. To each plot, the corresponding best-fit line and corresponding correlation coefficient were computed. R_1 was chosen to be the minimum value of R' for which the correlation coefficient, C^2, was largest and at least as large as 98%. That is, R_1 and t_1 are the smallest values beyond which power-law behaviour was well-established. For the data shown in Figure 4, we found $R_1 \simeq 3.1\,(\pm\,0.2)$ cm and $t_1 \simeq 5.0\,(\pm\,0.1)$ s.

In this, as in most experiments, we found that the front position obeys a power law over tens of seconds. Explicitly, for the data in Fig. 4, we found $R_f - R_1 \simeq 0.94\,(\pm\,0.01)\,(t - t_1)^{0.780\,(\pm\,0.004)}$. The error in the exponent was determined from the error of the best-fit line. However, azimuthal instability and differences in the power computed from the leftward and rightward propagating fronts observed from the sideview of the intrusion resulted in a larger error on the exponent of ± 0.15.

For $t \gtrsim 30$ s, the front advanced at a slower rate as it spread in the viscous-inertia regime. Although we are not concerned here with the rate of advance in this regime, we do examine the structure of the intrusion in both the buoyancy-inertia and viscous-inertia regimes.

To measure the variation of the thickness in time at a particular radial position, vertical time series were constructed from a sequence of vertical slices through successive snapshots of the experiment taken at some radius, r (not shown). In particular, we used vertical time series at $r = R_1$ to determine the intrusion top-to-bottom thickness, $h_1(t)$, over time at the location where the intrusion first formed. This is shown in Figure 5 as computed for the experiment shown in Fig. 2(c). At early times for a short period the height of the intrusion rapidly increased then leveled off and remained constant with a mean value, $h_1 = 4.0\,(\pm\,0.2)$ cm, even as the intrusion front advanced in the viscous-inertia regime. This near-constant long-time value of h_1 was observed in all our experiments.

Finally, the thickness of the intrusion, $h(r, t)$, as a function of radius, r, and time, t, was computed by matching contours to side-view snapshots of the leftward and rightward propagating intrusion at different times shown in Figs. 2(b) and 2(c). Using measured values of h_f and R_f, we are able to demonstrate that the intrusion head adopts a self-similar structure. This will be discussed in Sec. IV.

IV. RESULTS

Our experiments examined the spread height and consequent evolution of a radial intrusion resulting from the collapse of a plume/fountain in a stratified fluid.

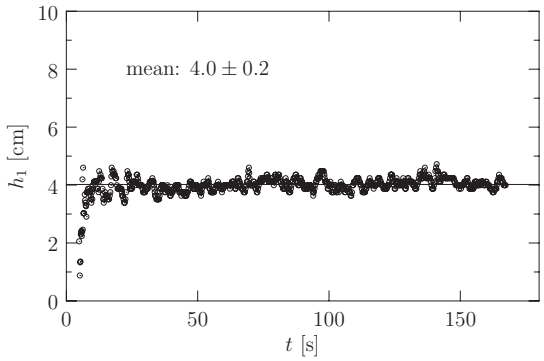

FIG. 5. Plot of the intrusion thickness, h_1, at radial distance R_1 versus time.

First, we examine the factors that determine the spreading height, Z_s, and the maximum steady-state height, Z_m, of the plume. Generally, we find that Z_s scales with Z_m. This is shown in Figure 6, which plots Z_{sv} vs Z_{mv} (the spreading and maximum heights with respect to a virtual origin) for a wide range of experiments. The slope of the best-fit line through the data implies that the intrusion spreads at a height,

$$Z_{sv} \simeq [0.66\ (\pm 0.014)]\ Z_{mv}. \tag{22}$$

In a small number of experiments we performed with $\sigma > 50$ (open triangles in Fig. 6), we found a moderately smaller slope of 0.5, consistent with the observations of Bloomfield and Kerr[17] in their experiments of fountains in stratified fluid.

Because Z_m depends upon the plume source conditions (M_0 and F_0) and the ambient stratification (N), we expect Z_s should likewise scale with these parameters. We examine this dependency by plotting the ratio Z_s/H_p (with H_p defined by (5)) against σ (defined by (7)) for all experiments. The results are shown in Figure 7.

For large σ, the results show that Z_s/H_p is related to σ through the power law relationship

$$f(\sigma) = [1.45(\pm 0.16)]\sigma^{-0.25\ (\pm 0.02)},\ \text{for}\ \sigma > 50, \tag{23}$$

consistent with the theory for momentum-dominated source conditions. The empirical result is consistent with the experiments of Bloomfield and Kerr[17] shown in this figure.

For smaller σ, the best-fit line through our data gives the power law relationship

$$f(\sigma) = [2.73(\pm 0.04)]\sigma^{-0.37(\pm 0.01)},\ \text{for}\ \sigma < 50. \tag{24}$$

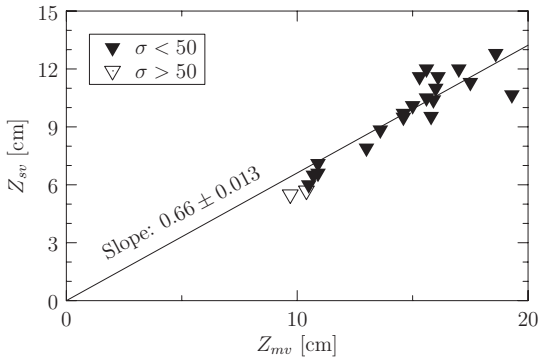

FIG. 6. The spread depth, Z_{sv}, plotted against the maximum steady state depth, Z_{mv}, of forced plumes for experiments with $\sigma < 50$ (filled triangles) and $\sigma > 50$ (open triangles). Both depths are given with respect to the virtual origin of the force plume. The best-fit line passing through the origin for values with $\sigma < 50$ is shown.

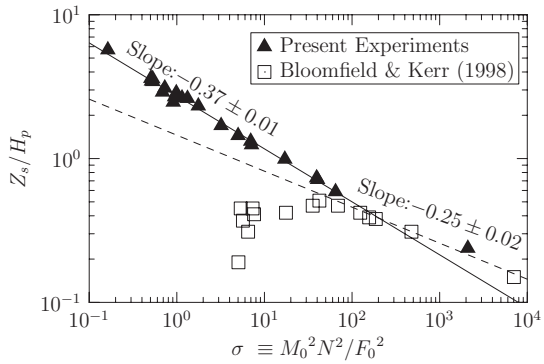

FIG. 7. The ratio of spread height, Z_s, to plume length scale, H_p plotted against σ for all our experiments and the experiments of Bloomfield and Kerr (1998), The dashed and solid lines represent the best-fit lines computed through our experimental data for $\sigma > 50$ and $\sigma < 50$, respectively.

This is consistent with the predicted 3/8 exponent for buoyancy-dominated source conditions. The fit is remarkably good considering that this prediction was strictly valid only in the limit, $\sigma \ll 1$, in theory.

The experiments of Bloomfield and Kerr[13,17] with $\sigma < 50$ differ significantly from ours because their source was negatively buoyant and so collapsed to the same horizontal level of the source. If there was insufficient source momentum to allow the fountain to mix with the ambient, then their results would reflect a similar power law relationship when σ is small. In this regard, it is remarkable that the scaling for large σ is well-predicted whether F_0 is positive or negative.

Having determined the empirical relationship between the spreading and maximum rise heights, we may compare our results with experiments examining the maximum rise heights of jets and pure plumes in stratified fluid. List[26] summarized these results giving the respective empirical predictions (recast in the notation of our paper) $Z_m/H_p \simeq 3.8\sigma^{-1/4}$ for $\sigma \gg 1$ and $Z_m/H_p \simeq 3.8\sigma^{-3/8}$ for $\sigma \ll 1$. Using (22) to find $Z_s/H_p \equiv f(\sigma)$, the proportionality constant is 2.51 ± 0.05. This is consistent with the coefficient we found in the small σ (buoyancy-dominated) limit. But it is almost double the value that we and Bloomfield and Kerr[17] found in the large σ (momentum-dominated) limit. The larger value may be attributed to the relatively small number of experiments, crude measurement methods, and conversion of data to σ and H_p variables.[26,28,29]

We denote by R_1 the radial distance from the centerline of the plume that is identified with the start of the intrusion in the buoyancy-inertia regime. In Figure 8, we plot the ratio of R_1/R_0 for a range of experiments with different σ. The plot shows no obvious dependence of R_1/R_0 upon whether the

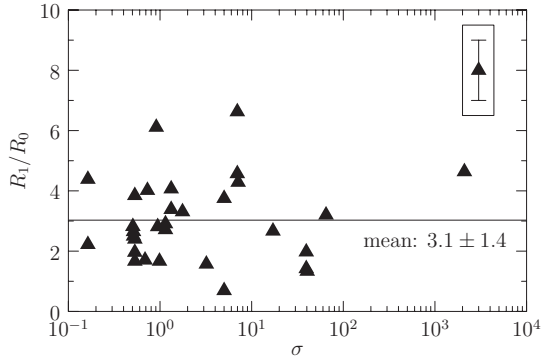

FIG. 8. The relative intrusion starting radius, R_1/R_0, versus σ. The horizontal line shows the mean value for all σ. Typical error bars are indicated in the boxed symbol to the upper-right of plot.

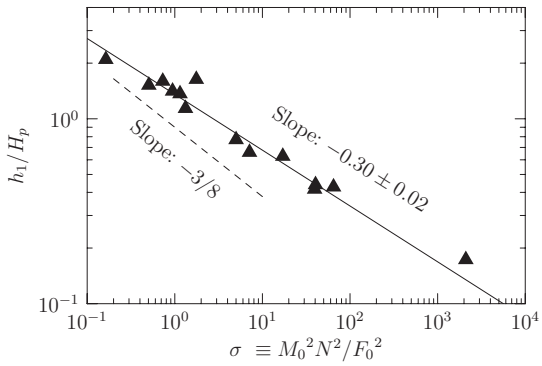

FIG. 9. The intrusion thickness at R_1 relative to H_p versus σ. The (solid) best-fit line through all the points is shown. The offset dashed line shows the slope of $-3/8$.

source flow is buoyancy- or momentum-driven. An average of the data in all experiments gives

$$R_1 \simeq [3.0\ (\pm 1.4)]\ R_0. \tag{25}$$

There is a lot of scatter in the data, in part as a consequence of errors in the determination of R_0 and the statistical analysis used to determine R_1.

For given R_1, we measure the thickness, h_1, of the intrusion at this location. As in the case shown in Figure 5, we find that h_1 is approximately constant in time shortly after the intrusion becomes established. The values of h_1 computed from a range of experiments are plotted in Figure 9. Here, h_1 is normalized by H_p and plotted against σ. The error associated with h_1/H_p is of the order 0.01, much smaller than the measured values. The log-log plot clearly shows the intrusion depth gets smaller with increasing σ. Explicitly, for $\sigma < 50$, we find

$$h_1 = H_p[1.36\ (\pm 0.06)]\,\sigma^{-0.30\ (\pm 0.02)}. \tag{26}$$

The exponent of -0.30 is found by finding the best-fit line through all the points. For $\sigma \ll 1$, we expect the source momentum flux, M_0, should not play a role and, such as Z_{sv}, we expect h_1, to scale as $H_p\sigma^{-3/8} = (F_0/N^3)^{1/4}$ independent of M_0. It may be that errors associated the measurement of h_1 could explain the discrepancy. Indeed the dashed line of slope $-3/8$ in Figure 9 indicates that values of h_1 in experiments with low σ are not inconsistent with a $-3/8$ power.

Figure 10 shows the power law exponent, P_r, which determines the slope of the front position versus time of the intrusion spreading in the inertia-buoyancy regime. Explicitly, each point was computed from the slope of the best-fit line through log-log plots of $(R_f - R_1)/R_1$ versus $N(t - t_1)$ (e.g., see Figure 4). The value of the resulting power law exponent, P_r, varies between 0.6

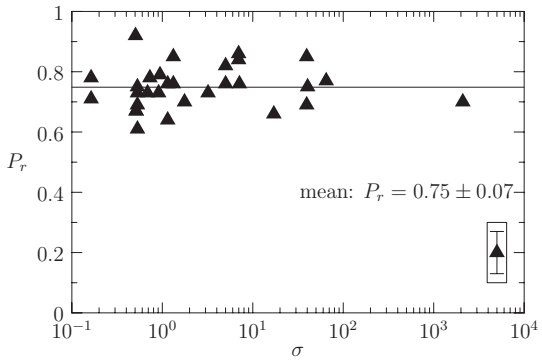

FIG. 10. The best-fit power law exponent, P_r, for the intrusion front position versus time plotted versus σ. Explicitly, P_r appears in the relation $\Delta R_f \propto \Delta t^{P_r}$ with $\Delta R_f \equiv R_f - R_1$ and $\Delta t \equiv t - t_1$. A typical error bar is indicated in the lower right-hand corner of the plot. The mean value of all data is indicated by the horizontal line.

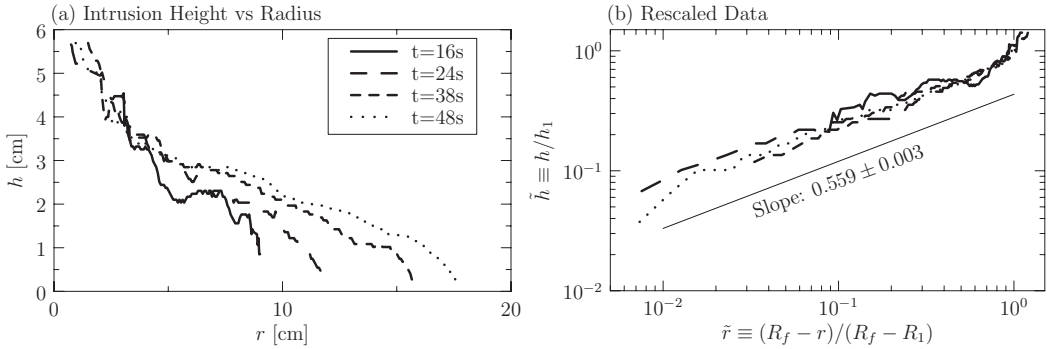

FIG. 11. (a) Plot of the intrusion thickness, h, as a function of radial distance, r, for times $t = 16$, 24, 38, 48 s. (b) Corresponding log-log plots of the normalized height, $\tilde{h} = h/h_1$ versus the normalized radius, $\tilde{r} = (R_f - r)/(R_f - R_1)$. Results are computed for the same experiment shown in Fig. 2. The solid diagonal line is the vertically offset best-fit line through the four collapsed curves.

and 0.95, but shows no obvious dependence upon σ. Averaging the results for all experiments gives $P_r \simeq 0.75\,(\pm 0.07)$. The large error in the exponent was dominated by statistical analysis used to determine R_1. The intercept of the best-fit line is used to find the nondimensional coefficient. This value is found to scale approximately as $L_F = (F_0/N^3)^{1/4}\,(= H_p\sigma^{-3/8})$, consistent with the scaling predicted by (16). Explicitly, we find

$$R_f - R_1 \simeq [0.33\ (\pm 0.03)]\ L_F\ [N(t - t_1)]^{[0.75(\pm 0.07)]}. \tag{27}$$

We now consider the shape of the intrusion. Figure 11(a) shows profiles of the intrusion thickness, $h(r; t)$, as a function of radial distance, r, determined from side view snapshots of the experiment shown in Fig. 2. The profiles are plotted only for times $t = 16$, 24, 38, 48 s. Generally, we found that the thickness of the intrusion decreased with increasing radius, but the thickness at R_1 changed little over time, consistent with Fig. 11.

Having computed the values of h_1 and R_1, and knowing the front position as a function of time, $R_f(t)$, we define a rescaled nondimensional height by $\tilde{h} = h/h_1$ and a rescaled nondimensional radial co-ordinate by $\tilde{r} = (R_f - r)/(R_f - R_1)$. Generally, we find that the rescaled profiles of $\tilde{h}(\tilde{r}; t)$ computed for a wide range of times collapse reasonably well onto a single curve. This is illustrated in Figure 11(b), which shows the rescaled data from Fig. 11(a) on a log-log plot. That the data collapse onto a single curve indicates the intrusion structure is self-similar, but with constant thickness, $h = h_1$, at $r = R_1$. A best-fit line through the log-log plots of the four curves gives a power law of the form, $\tilde{h} \propto \tilde{r}^{P_h}$, satisfying $\tilde{h}(0) = 0$ and $\tilde{h}(1) = 1$.

Figure 12 shows that the power law exponent, P_h, does not vary significantly with σ. Its value, computed for six different experiments with σ ranging from 1 to 2100, is $P_h \simeq 0.55\,(\pm\ 0.03)$.

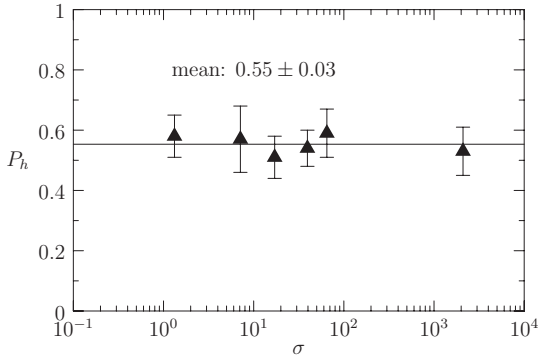

FIG. 12. Power law exponent, P_h, of rescaled intrusion height profile determined in experiments with six values of σ.

Explicitly, we find the relation

$$\frac{h}{h_1} \sim \left(\frac{R_\mathrm{f} - r}{R_\mathrm{f} - R_1}\right)^{0.55\ (\pm 0.03)}. \tag{28}$$

This empirical result supports the theoretical assumption that the intrusion thickness as a function of radius may be represented by (18). However, a consequence of this assumption, together with assumptions that the volume or buoyancy flux is constant, is that the intrusion front should advance linearly in time near the source and as the square root of time in the far field (21). With $P_h \simeq 0.55$, the transition between these asymptotic regimes is predicted to occur at radius $R_{\mathrm{f}c} \simeq 4.1R_1 \simeq 12R_0$ for $R_1 = 3R_0$.

In our experiments, the buoyancy-inertia regime was observed to extend for $R_1 \lesssim R_f \lesssim 10R_{\mathrm{f}c}$ (e.g., see Figure 4). In light of this observation and because the power law fits that resulted in the exponents in Figure 10 extend over this range, it is not clear that the front position truly advances as a 3/4 power of time. The front could advance more quickly at early times and more slowly in the inertia-buoyancy regime at later times. But the inherent noise of these experiments did not allow us to observe such a transition, if indeed it exists.

V. DISCUSSION AND CONCLUSIONS

We have examined the height, Z_s, radial advance, $R_\mathrm{f}(t)$, and thickness, $h(r, t)$, of a radial intrusion resulting from the collapse of a forced plume in uniformly stratified fluid. The spreading height was predicted as a function of the ambient stratification, the source momentum and buoyancy fluxes. Explicitly, from (23) and (24), we found

$$Z_\mathrm{s} \simeq \begin{cases} 2.7\ (F_0/N^3)^{1/4}, & M_0/F_0 \lesssim 7N^{-1} \\ 1.5\ (M_0/N^2)^{1/4}, & M_0/F_0 \gtrsim 7N^{-1} \end{cases}. \tag{29}$$

The power laws are consistent with expectations from the theory based upon the asymptotic limits of $M_0N/F_0 \ll 1$ and $\gg 1$.

The radial position of the intrusion front was found to depend upon time closer to a power of $P_r \sim 3/4$ instead of 2/3 power law. This is consistent with other experiments[21,23] and theory that requires constant buoyancy flux instead of the volume flux of an intrusion spreading in uniformly stratified fluid. However, the self-similar shape of the intrusion, together with the observed restriction that the intrusion thickness is fixed in time at its source, dictates according to (21), that the intrusion speed should first advance linearly in time and then as a square-root of time. Given the power law exponent determining the head shape was $P_h \simeq 0.55$, the transition from linear to square-root dependence is predicted to take place when the front position is at $R_f \simeq 4R_1$. This transition position is in the middle of the range of R_f over which the power law exponent P_r was determined. And so it is unclear whether the intrusion exhibited self-similar behaviour resulting from a constant buoyancy flux as in the approximations leading to (16), or whether it exhibited a transition from near-to-far plume evolution as in (21).

Both predictions assumed a constant buoyancy flux at the source of the intrusion (at $r = R_1$). But this may not be the case. The theories presented here have ignored the modification of the ambient stratification and opposing velocities induced by the radially advancing intrusion. Such radially-inward motions of enhanced stratification could modify the entrainment associated with the fountain and so change the source conditions for the intrusion. Much larger scale experiments and more sophisticated analyses are required to address these issues.

Despite these uncertainties, it is a useful exercise to consider how our results apply to observed volcanic explosions that extend well into the stratosphere and are not significantly affected by background winds. A large volcanic plume can penetrate tens of kilometers into the stratosphere.[2,34,40,41] It then collapses and ultimately spreads as an intrusion with thickness[2,8] ranging from 1 km to 2 km.

In the extreme case of the June 15, 1991, Mount Pinatubo eruption, satellite observations revealed[34] that the eruption column extended upwards to a maximum height of $Z_\mathrm{m} \sim 40$ km. With the radius of the eruption column at its source taken to be on the order $b_0 = 1$ km, the virtual origin

is taken to be approximately 4 km below the surface. Thus, using (22), we estimate the intrusion should have spread around 25 km altitude.

The momentum and buoyancy fluxes across the tropopause provide the initial conditions for the plume entering the stratosphere.[18] If we assume that the buoyancy flux dominates over the momentum flux at the tropopause (near 16 km altitude), then taking $N = 0.017\,\mathrm{s}^{-1}$ in the stratosphere[34] and using (29), we estimate the buoyancy flux at the virtual origin to be $F_0 = 1.2 \times 10^{11}\,\mathrm{m}^4/\mathrm{s}^3$. Assuming the stratification of the troposphere is negligible, this would also be the buoyancy flux at the tropopause. If the momentum flux dominates, we find $M_0 = 5.3 \times 10^{12}\,\mathrm{m}^4/\mathrm{s}^2$. Assuming the buoyancy flux is negligible, this would also be the momentum flux at the tropopause. Below we will see that observations of the intrusion speed and thickness, imply that the eruption was, in fact, momentum-dominated at the tropopause.

The umbrella cloud emanating from the Pinatubo eruption was observed to propagate radially away at a speed as fast as $u_1 \simeq 20$ m/s near the start of the inertia-buoyancy regime.[34] This surpassed the local stratospheric wind speeds, so that ambient winds did not significantly affect the intrusion evolution at least during the early stages of its propagation in the buoyancy-inertia regime. Indeed, the spread was observed to be symmetrical about the eruption column for the first 4–5 h over which time it spreads radially 300 km from the source.[34]

Taking $N = 0.017\,\mathrm{s}^{-1}$ and using (9), with $\mathrm{Fr} = 0.3$ gives an estimate for the intrusion thickness[34] of $h_1 \simeq 4$ km. This is consistent with the observed thickness[41] that ranged between 3 km and 6 km.

The first satellite observation of the Pinatubo eruption was estimated to be made 800 s after the initial explosion.[34] At this time the mean radius of the umbrella cloud was approximately 30 km. We take this as the value of R_1 which, using (25), is consistent with the estimated radius of the central eruption column, $R_0 \simeq 10$ km.

The volume flux at R_1 is estimated to be $Q_i = 2\pi R_1 h_1 u_1 \simeq 1.5 \times 10^{10}\,\mathrm{m}^3/\mathrm{s}$, which is of the order $5 \times 10^{10}\,\mathrm{m}^3/\mathrm{s}$ estimated indirectly by observations from satellite images.[41] Using (12), the buoyancy flux is $F_i = Q_i N^2 h_1 \simeq 1.7 \times 10^{10}\,\mathrm{m}^4/\mathrm{s}^3$. Comparing these results with the above estimated values of F_0 and M_0 for plumes dominated by buoyancy-flux and momentum-flux, respectively, we see that F_0 is only moderately larger than F_i. If the flow was buoyancy dominated at the tropopause, we would expect significantly reduced buoyancy flux associated with the intrusion: $F_0 \gg F_i$. This not being the case, we expect the plume was momentum-dominated with $M_0 \simeq 5.3 \times 10^{12}\,\mathrm{m}^4/\mathrm{s}^2$ at the tropopause, situated at $z \simeq 16$ km.

Observations of the Pinatubo plume spread[34] indicate that the radius increased as $R(t) \propto t^{0.65(\pm 0.01)}$ for distances out to 600 km. The power law is consistent with the box-model prediction (11) assuming a constant volume flux, Q_i. But it differs from our experimental results that show on average the intrusion radius increases as $t^{0.75(\pm 0.07)}$. Given that entrainment of ambient air into the Pinatubo umbrella cloud was evident from photographs, it seems unlikely that this intrusion could be well-modelled as having a constant volume flux at radius R_1. One reason for the discrepancy could be that R_1 (and t_1) were incorrectly estimated from the satellite observations. Alternately, it may be that particles in the flow significantly alter the buoyancy flux within the umbrella cloud.

As an aside, we also briefly consider the application of our results to the spreading of oil at depth resulting from the 2010 Deepwater Horizon blowout in the Gulf of Mexico. Crudely modelling the source as a jet with opening on the scale of $b_0 = 0.1$ m and volume flux $0.1\,\mathrm{m}^3/\mathrm{s}$ (about 55 000 barrels per day), the source momentum flux is of the order $M_0 \sim 1\,\mathrm{m}^4/\mathrm{s}^2$. Further assuming the stratification at depth is of the order $N \sim 10^{-3}\,\mathrm{s}^{-1}$, (29) predicts a spreading height around $Z_s = 50$ m above the source. In fact, observations revealed that the oil from the plume spread laterally 200–500 m above the source.[42,43] The discrepancy is attributed to the multiphase dynamics (e.g., gas bubbles, oil droplets, gas hydrates) which significantly change the buoyancy of deep water oil spills throughout the whole evolution of the rising jet, collapsing fountain, and spreading intrusion.[44]

Likewise, in applying our results to volcanic eruptions we neglected the dynamics of hot particles and moisture entrainment within the eruption column. In this regard, the experiments act primarily as a means to gain meaningful insights into the dynamics of radially spreading forced plumes. From this foundation further studies will be conducted to investigate the effects of particle size variation in the rise and spread of turbulent plumes in stratified fluid. We will proceed by studying the deposition

of differently sized particles falling out of a turbulent force plume as it rises and spreads at its neutral buoyancy level.

ACKNOWLEDGMENTS

Bruce R. Sutherland would like to thank Gabriel Rooney (UK Meteorological Office) and Paul Linden (U. Cambridge) for their inspiration to examine this problem. Particular thanks to Andrew Hogg (U. Bristol), Paul Linden (U. Cambridge), and Andrew Woods (U. Cambridge) for their insightful comments regarding the theoretical interpretation of this work.

Part of this research was conducted by Quentin Aubourg as a Research Assistant during a four-month visiting internship to the University of Alberta from the University of Grenoble. This work was supported by funding from the Natural Sciences and Engineering Research Council Discovery Grant program, RGPIN 203065.

[1] A. Costa, A. Folch, and G. Macedonio, "A model for wet aggregation of ash particles in volcanic plumes and clouds: 1. Theoretical formulation," J. Geophys. Res. **115**, B09201, doi:10.1029/2009JB007175 (2010).
[2] P. G. Baines and R. S. J. Sparks, "Dynamics of giant volcanic ash clouds from supervolcanic eruptions," Geophys. Res. Lett. **32**, L24808, doi:10.1029/2005GL024597 (2005).
[3] R. Sparks, S. Carey, J. Gilbert, L. Glaze, H. Sigurdsson, and A. Woods, *Volcanic Plumes* (John Wiley, Chichester, 1997).
[4] D. B. Williams and H. E. Thomas, "An assessment of volcanic hazards to aviation," Geomatics. Natural, Hazards Risk **2**, 233–246 (2011).
[5] A. Costa, G. Macedonio, and A. Folch, "A three-dimensional Eulerian model for transport and deposition of volcanic ashes," Earth Planet. Sci. Lett. **241**, 634–647 (2006).
[6] L. Wilson, R. S. J. Sparks, T. C. Huang, and N. D. Watkins, "The control of volcanic column heights by eruption energetics and dynamics," J. Geophys. Res. **83**, 1829–1836, doi:10.1029/JB083iB04p01829 (1978).
[7] R. E. Holasek, A. W. Woods, and S. Self, "Experiments on gas-ash separation processes in volcanic umbrella plumes," J. Volcanol. Geotherm. Res. **70**, 169–181 (1996).
[8] R. S. J. Sparks, J. G. Moore, and C. J. Rice, "The initial giant umbrella cloud of the May 18, 1980 eruption of Mount St-Helens," J. Volcanol. Geothermal Res. **28**, 257–274 (1986).
[9] C. Textor, H. F. Graf, M. Herzog, J. M. Oberhuber, W. I. Rose, and G. Ernst, "Volcanic particle aggregation in explosive eruption column. Part I: Parameterization of the microphysics of hydrometeors and ash," J. Volcanol. Geothermal Res. **150**, 359–377 (2006).
[10] A. W. Woods, "Turbulent plumes in nature," Annu. Rev. Fluid Mech. **42**, 391–412 (2010).
[11] B. R. Morton, G. I. Taylor, and J. S. Turner, "Turbulent gravitational convection from maintained and instantaneous sources," Proc. R. Soc. London, Ser. A **234**, 1–23 (1956).
[12] T. J. McDougall, "Negatively buoyant vertical jets," Tellus **33**, 313–320 (1981).
[13] L. J. Bloomfield and R. C. Kerr, "A theoretical model of a turbulent fountain," J. Fluid Mech. **424**, 197–216 (2000).
[14] B. R. Morton, "Coaxial turbulent jets," Int. J. Heat Mass Transf. **5**, 955–965 (1962).
[15] J. S. Turner, "Jets and plumes with negative or reversing buoyancy," J. Fluid Mech. **26**, 779–792 (1966).
[16] G. G. Rooney and B. J. Devenish, "Plume rise and spread in a linearly stratified environment," Geophys. Astrophys. Fluid Dyn. (published online).
[17] L. J. Bloomfield and R. C. Kerr, "Turbulent fountains in a stratified fluid," J. Fluid Mech. **358**, 335–356 (1998).
[18] J. K. Ansong and B. R. Sutherland, "Internal gravity waves generated by convective plumes," J. Fluid Mech. **648**, 405–434 (2010).
[19] T. Maxworthy, "Experimental and theoretical studies of horizontal jets in a stratified fluid," in *Proceedings of the International Symposium on Stratified Flows* (International Association for Hydraulic Research, Novosibirsk, Russia, 1972), pp. 611–618.
[20] H. E. Huppert and J. E. Simpson, "The slumping of gravity currents," J. Fluid Mech. **99**, 785–799 (1980).
[21] N. Didden and T. Maxworthy, "The viscous spreading of plane and axisymmetric gravity currents," J. Fluid Mech. **121**, 27–42 (1982).
[22] G. N. Ivey and S. Blake, "Axisymmetric withdrawal and inflow in a density-stratified container," J. Fluid Mech. **161**, 115–137 (1985).
[23] N. Kotsovinos, "Axisymmetric submerged intrusion in stratified fluid," J. Hydraulic Eng. ASCE **126**, 446–456 (2000).
[24] A. W. Woods, "A note on non-Boussinesq plumes in an incompressible stratified environment," J. Fluid Mech. **345**, 347–356 (1997).
[25] H. C. Burridge and G. R. Hunt, "The rise heights of low- and high-Froude-number turbulent axisymmetric fountains," J. Fluid Mech. **691**, 392–416 (2012).
[26] E. J. List, "Turbulent jets and plumes," in *Mixing in Inland and Coastal Waters*, edited by H. B. Fischer, E. J. List, R. C. Y. Koh, J. Imberger, and N. H. Brooks (Academic Press Inc., San Diego, 1979), pp. 315–389.
[27] B. R. Morton, "Forced plumes," J. Fluid Mech. **5**, 151–163 (1959).
[28] L.-N. Fan, "Turbulent buoyant jets into stratified or flowing ambients," Ph.D. thesis (California Institute of Technology, 1967).
[29] D. G. Fox, "Forced plume in stratified fluid," J. Geophys. Res. **75**, 6818–6835, doi:10.1029/JC075i033p06818 (1970).

[30] C. P. Caulfield and A. W. Woods, "Plumes with non-monotonic mixing behaviour," Geophys. Astrophys. Fluid Dyn. **79**, 173–199 (1995).
[31] M. Ungarish, "On gravity currents in a linearly stratified ambient: A generalization of Benjamin's steady-state propagation results," J. Fluid Mech. **548**, 49–68 (2006).
[32] B. R. Sutherland, A. N. F. Chow, and T. P. Pittman, "The collapse of a mixed patch in stratified fluid," Phys. Fluids **19**, 116602-1–116602-6 (2007).
[33] D. Bolster, A. Hang, and P. F. Linden, "The front speed of intrusions into a continuously stratified medium," J. Fluid Mech. **594**, 369–377 (2008).
[34] R. E. Holasek, S. Self, and A. W. Woods, "Satellite observations and interpretation of the 1991 Mount Pinatubo eruption plumes," J. Geophys. Res. **101**, 27635–27655, doi:10.1029/96JB01179 (1996).
[35] J. Chen, "Studies on gravitationally spreading currents," Ph.D. thesis (California Institute of Technology, 1980).
[36] C. Lemckert and J. Imberger, "Axisymmetric intrusive gravity currents in linearly stratified fluids," J. Hydraulic Eng. ASCE **119**, 662–679 (1993).
[37] P. F. Linden, private communication (2013).
[38] G. Oster, "Density gradients," Sci. Am. **213**, 70 (1965).
[39] J. Lee and V. Chu, *Turbulent Buoyant Jets and Plumes: A Langrangian Approach* (Kluwer Academic Publishers, Dordrecht, The Netherlands, 2003).
[40] T. Koyaguchi and M. Tokuno, "Origin of the giant eruption cloud of Pinatubo, June 15, 1991," J. Volcanol. Geotherm. Res. **55**, 85–96 (1993).
[41] T. Koyaguchi, "Grain-size variation of tephra derived from volcanic umbrella clouds," Bull. Volcanol. **56**, 1–9 (1994).
[42] R. Camilli, C. M. Reddy, D. R. Yoerger, B. A. S. V. Mooy, M. V. Jakuba, J. C. Kinsey, C. P. McIntyre, S. P. Sylva, and J. V. Maloney, "Tracking hydrocarbon plume transport and biodegradation at deepwater horizon," Science **330**, 201–204 (2010).
[43] A. Adcroft, R. Hallberg, J. P. Dunne, B. L. Samuels, J. A. Galt, C. H. Barker, and D. Payton, "Simulations of underwater plumes of dissolved oil in the Gulf of Mexico," Geophys. Res. Lett. **37**, L18605, doi:10.1029/2010GL044689 (2010).
[44] P. D. Yapa and L. Zheng, "Modelling oil and gas releases from deep water: A review," Spill Sci. Tech. Bull. **4**, 189–198 (1997).